Investigating the collector efficiency of silver nanofluids based direct absorption solar collectors

Meijie Chen[1], Yurong He[1*], Jiaqi Zhu[1], Dongsheng Wen[2]

[1] *Harbin Institute of Technology, Harbin, China, 150001*

[2]*University of Leeds, Leeds, UK, LS2 9JT*

Abstract: A one-dimensional transient heat transfer analysis was carried out to analyze the effects of the Nanoparticle (NP) volume fraction, collector height, irradiation time, solar flux, and NP material on the collector efficiency. The numerical results were compared with the experimental results obtained by silver nanofluids to validate the model, and good agreement was obtained. The numerical results show that the collector efficiency increases as the collector height and NP volume fraction increase and then reaches a maximum value. An optimum collector height (~ 10 mm) and particle concentration (~ 0.03%) achieving a collector efficiency of 90% of the maximum efficiency can be obtained under the conditions used in the simulation. However, the collector efficiency decreases as the irradiation time increases owing to the increased heat loss. A high solar flux is desirable to maintain a high efficiency over a wide temperature range, which is beneficial for subsequent energy utilization. The modeling results also show silver and gold nanofluids obtain higher photothermal conversion efficiencies than the titanium dioxide nanofluid because their absorption spectra are similar to the solar radiation spectrum.

Keywords: Solar energy; Silver nanofluid; Direct solar absorption collector; Collector efficiency

1. Introduction

The increases in both the global population and living quality have increased the demand for electricity, but the amount of fossil fuels is limited. Moreover, the combustion of fossil fuels has resulted in many environmental concerns such as the greenhouse effect due to carbon dioxide emission and acid rain produced by acid gas emission [1,2]. Hence, the development of efficient sustainable energy is currently one of the most important challenges. Solar energy, as a clean and sustainable energy source, provides a potential solution to this challenge. For instance, the solar energy that reaches the Earth's surface over one hour is greater than the worldwide energy consumption for one year [3,4]. The challenges for solar energy lie in the effective absorption, conversion, and storage of solar radiation, which are significantly affected by the working medium [5-8]. To simplify the collector and enhance its efficiency, a so-called Direct Solar Absorption Collector (DASC) has been proposed [9]. Compared with a surface-based collector, the DASC directly absorbs solar radiation in a bulk fluid, and the temperature distribution becomes more uniform, resulting in a small heat loss at the capture surface [10]. In a DASC, solar energy is

[*]Corresponding author address: School of Energy Science & Engineering, Harbin Institute of Technology, China, 150001. Tel: +86 451 86413233.

E-mail address: rong@hit.edu.cn (Y. He)

directly absorbed and then transferred by the working fluid. Hence, the working fluid needs to have good optical performance to maximize the absorption of solar energy and possess excellent heat transfer capabilities to decrease the temperature difference [11].

The application of a nanofluid as the working fluid of a DASC is a relatively new concept in the last decade [12,13], which was first demonstrated by Tyagi et al. [14]. Nanoparticles (NPs) dispersed in a base fluid offer the potential to improve the optical properties of nanofluids, which could lead to an increase in the collector efficiency due to the absorption and scattering of NPs. Additionally, it has been shown that the addition of NPs has a dramatic effect on the base fluid's thermophysical properties such as the thermal conductivity, mass diffusivity, and viscosity [15-20]. Compared with the base fluid, the enhanced optical and thermophysical properties of a nanofluid allow it to be a working medium applied in different solar collectors [21,22]. Tyagi et al. [14] revealed that under similar operating conditions, the efficiency of a DASC using nanofluids as the working fluid was up to 10% higher than that of a flat-plate collector. In addition, they also observed that the presence of NPs increased the absorption of solar energy by more than nine times compared to that of pure water. Many recent studies have indicated that the selection of the nanofluid is very important to obtain a performance enhancement in a DASC. A carbon nanotube/water nanofluid was applied as a working fluid in low-temperature DASCs by Karami et al. [23]. The extinction coefficient and thermal conductivity of the functionalized carbon nanotube nanofluid showed remarkable improvement compared to the base fluid, even at low particle loadings. Its promising optical and thermal properties, together with the appropriate stability, make it very interesting for increasing the overall efficiency of low-temperature DASCs. The extinction coefficient of a water-based aluminum nanofluid with a varying NP size and volume fraction was investigated and evaluated by Saidur et al. [24]. The particle size had a minimal influence on the optical properties of the nanofluid. Moreover, a promising improvement was achieved within a volume fraction of 1.0%, and the nanofluid was almost opaque to light. The optical properties of a titanium dioxide nanofluid for a DASC was studied by Said et al. [25]. Promising results were observed for NP volume fractions less than 0.1%. Despite having a very high extinction coefficient at shorter wavelengths, the addition of particles to water could also improve the light absorption ability in the visible- and shorter-wavelength regions. He et al. [26] experimentally investigated the photothermal properties of copper/water nanofluids. The results showed that the temperature of the copper/water nanofluids (0.1 wt.%) can be increased up to 25.3% compared with that of deionized water when the solar irradiation time was ~1200 s under natural sunlight. As stated above, different NP materials, NP volume fractions, and collector styles have significant impacts on the solar utilization efficiency. The selection of the working fluid is very important to obtain a performance enhancement in a DASC.

In recent years, the applications of plasmonic NPs for solar absorption have attracted significant interest [27-29]. Research has showed that silver NPs exhibit an excellent photothermal conversion capability, even at very low NP volume fractions since the Localized Surface Plasmon

Resonance (LSPR) in the nanostructures enhance the electric-field intensity, resulting in enhanced scattering and absorption coefficients at the LSPR frequency [30]. For the applications of plasmonic NPs, silver is the most attractive metal owing to its high surface plasmon strength, which allows silver nanofluids with very low concentrations to exhibit considerable absorption and scattering properties at the resonance frequency [31]. Further, many works have focused on the experimental determination or simulation of the optical properties of NPs for the application of plasmonic NPs to DASCs [27,28,32]. It should be noted that in addition to the properties of the working fluids, the parameters of a DASC also have strong impacts on the efficiency, which is a factor that has received little attention. A systemic simulation of the optical properties of the working medium and the collector parameters is significant for the application of plasmonic NPs to DASCs. To achieve an optimized collector efficiency, it is desirable to systematically investigate the photothermal conversion characteristics of plasmonic nanofluids under different conditions both experimentally and numerically, including different collector designs.

In this work, the photothermal conversion characteristics of plasmonic silver nanofluids for DASCs are investigated. Silver NPs are synthesized by using ascorbic acid as a reductant and citrate as a stabilizer. A one-dimensional transient heat transfer analysis is carried to analyze the effects of the NP volume fraction, collector height, irradiation time, solar flux, and NP material on the collector performance, leading to optimized collector and fluid parameters.

2. Numerical calculation

A one-dimensional (1-D) numerical analysis is developed to study a DASC undergoing transient heat conduction in the presence of natural convection on the top surface, as shown in Fig. 1. The nanofluid is contained within the enclosure of the collector. The length of the collector along the horizontal direction is assumed to be sufficiently large compared to the height h in the vertical direction. The bottom, left, and right side walls are considered to be adiabatic, i.e., no heat flux is allowed to pass through except for the transmitted radiation. The top surface consists of selective glass that allows most of the incident solar flux to pass through it. As the temperature of nanofluid is low, the heat loss from the top surface exposed to the ambient atmosphere is mainly through convection. Therefore, only convection heat loss is considered for the top surface.

2.1 Solar radiation

The incident radiation is considered to be the incoming solar radiation. To consider the irradiated solar energy, it is necessary to know the values of the solar radiation intensity for the calculated wavelength. The atmospheric absorption is neglected in the following calculation. Hence, the incident solar intensity is calculated using the blackbody relation based on Planck's law, which describes the amount of electromagnetic energy at a certain wavelength radiated by a blackbody at thermal equilibrium. The relation is given as follows:

$$I_{b\lambda}(\lambda,T_{Solar})=\frac{2hc_0^2}{\lambda^5\left[\exp\left(\frac{hc_0}{\lambda k_B T_{Solar}}\right)-1\right]} \tag{1}$$

where $I_{b\lambda}$ is the spectral intensity of the blackbody, h is Planck's constant, k_B is the Boltzmann constant, c_0 is the speed of light in vacuum, λ is the wavelength, and T_{Solar} is the solar temperature, which is taken as 5800 K. The incident solar heat flux is modified to CG, where C is the modification factor, and G is the heat flux radiated by a blackbody at 5800 K. The air mass is 1.5 (i.e., AM = 1.5), which represents the solar spectrum at the mid-latitudes, and the solar intensity is 1000 W/m^2 according to the ASTM G-173 standard. The value of C is taken as 0.74 to match the solar intensity at AM = 1.5. The spectral radiant intensity versus the wavelength is shown in Fig. 2, and the solar intensity is 1000 W/m^2 after the integral calculation.

2.2 Radiative properties

When radiation passes through a medium, its energy will be gradually reduced because of absorption and scattering. The Radiative Transfer Equation (RTE) describes the interrelation among emission, absorption, scattering, and transmission when the radiation energy passes through a medium. It is an energy-balance equation along the direction of the propagating radiation, which is expressed as follows [33]:

$$\frac{\mathrm{d}I_\lambda(\mathbf{s})}{\mathrm{d}\mathbf{s}}=-k_{a\lambda}I_\lambda(\mathbf{s})-k_{s\lambda}I_\lambda(\mathbf{s})+k_{a\lambda}I_{b\lambda}(\mathbf{s})+\frac{k_{s\lambda}}{4\pi}\int_{4\pi}I_\lambda(\mathbf{s},\mathbf{\Omega}')\Phi_\lambda(\mathbf{\Omega},\mathbf{\Omega}')\mathrm{d}\mathbf{\Omega}' \tag{2}$$

where I_λ is the spectral intensity, $\mathbf{s}$ is the vector of the location, $k_{a\lambda}$ is the spectral absorption coefficient, $k_{s\lambda}$ is the spectral scattering coefficient, $\mathbf{\Omega}$ and $\mathbf{\Omega}'$ are the directions of radiative transfer, and Φ_λ is the spectral scattering phase function. When the NP volume fraction is less than 0.1%, it is possible to neglect the directional dependence of the radiation, and only one dimension is considered. Since the fluid temperature in the collector is not very high, the emission term is excluded. The scattering efficiency of the nanofluid is proportional to the biquadrate of the NP size, which will be described in Eq. (10). Moreover, the calculated particle sizes are within the nanoscale range. Therefore, to maintain a simple model, the RTE can be simplified as follows:

$$\frac{\partial I_\lambda}{\partial y}=-(k_{a\lambda}+k_{s\lambda})I_\lambda=-k_{e\lambda}I_\lambda \tag{3}$$

where $k_{e\lambda}$ is the spectral extinction coefficient. When the volume fraction of the NPs is less than 0.6 vol.% and the particle size is very small, the particles can be assumed to be in the independent scattering regime [34], which requires relatively simple calculations of the optical properties. The present model assumes independent scattering, where the scattered radiation does not depend on each other. Hence, the intensities can be added, and the extinction caused by the nanofluid could be obtained by adding the individual contributions from the NPs as well as the base fluid [14,24,25]. It can be calculated by considering the independent extinction coefficient as follows:

$$k_{e\lambda,nanofluid} = k_{e\lambda,basefluid} + k_{e\lambda,nanoparticles} \tag{4}$$

The complex refractive index *m* can describe the optical constant of the absorbing medium:

$$m_{medium} = n_{medium} + i\kappa_{medium} \tag{5}$$

where *n* is the refraction coefficient, and κ is the absorption coefficient.

Only absorption should be considered, and scattering can be neglected in a pure fluid. Thus, the spectral extinction coefficient of the base fluid (i.e., water) can be calculated by

$$k_{e\lambda,basefluid} \approx k_{a\lambda,basefluid} = \frac{4\pi\kappa_{basefluid}}{\lambda} \tag{6}$$

For nanofluids, where NPs are present in the base fluid, scattering and absorption have complex relationships. As the NP volume fraction is low (less than 0.1%) and the NP size is smaller than the wavelength of the incident radiation, the Rayleigh approximation can be used to describe NP absorption and scattering. This approximation is useful when the size parameter $\alpha < 1$, which is expressed as

$$\alpha = \frac{\pi D}{\lambda} \tag{7}$$

where *D* is the NP diameter. The relative complex refractive index of the NPs to the base fluid *m* is defined as follows:

$$m = \frac{m_{nanoparticles}}{n_{basefluid}} \tag{8}$$

On the basis of the Rayleigh approximation, the following relations for the absorption efficiency and scattering efficiency are used in the model:

$$k_{a\lambda,nanoparticles} = \frac{12\alpha f_v}{D}\mathrm{Im}\left\{\frac{m^2-1}{m^2+2}\left[1+\frac{\alpha^2}{15}\left(\frac{m^2-1}{m^2+2}\right)\frac{m^4+27m^2+38}{2m^2+3}\right]\right\} \tag{9}$$

$$k_{s\lambda,nanoparticles} = \frac{8\alpha^4 f_v}{D}\left|\frac{m^2-1}{m^2+2}\right| \tag{10}$$

Finally, the extinction of the nanofluid could be calculated on the basis of the wavelength, the NP volume fraction and diameter, and the main optical constants of the base fluid and NPs.

2.3 Governing equations

A transient energy equation coupled with the RTE (Eq. (3)) is adopted to predict the DASC performance. Moreover, the thermodynamic properties of the nanofluids are calculated by predictive models. The density of the nanofluid can be assumed to be equal to the base-fluid density because the NP volume fraction calculated in this model is very low and the effect of the NPs on the density can be neglected.

The specific heat of the nanofluids will change as NPs are added and can be modeled by the following equation [35]:

$$c_{p,nanofluid} = \frac{f_v \rho_{nanopartilces} c_{p,nanoparticles} + (1 - f_v)\rho_{water} c_{p,basefluid}}{f_v \rho_{nanoparticles} + (1 - f_v)\rho_{basefluid}} \tag{11}$$

where $c_{p,nanofluid}$, $c_{p,nanoparticles}$, and $c_{p,basefluid}$ are the specific heat capacities of the nanofluid, NP, and base fluid, respectively; and $\rho_{nanopartilces}$ and $\rho_{basefluid}$ are the densities of the NP and base fluid, respectively.

The thermal conductivity of the nanofluids changes with the NP volume fraction and temperature. The effect of the temperature can be neglected because the temperature of the nanofluids is low, and the effect of the NP volume fraction can be described by the following model [36]:

$$\frac{k_{nanofluid}}{k_{basefluid}} = \frac{2 + k_{nanoparticles}/k_{basefluid} + 2\left(k_{nanoparticles}/k_{basefluid} - 1\right) f_v}{2 + k_{nanoparticles}/k_{basefluid} - 2\left(k_{nanoparticles}/k_{basefluid} - 1\right) f_v} \tag{12}$$

where $k_{nanofluid}$, $k_{nanoparticles}$, and $k_{basefluid}$ are the thermal conductivities of the nanofluid, NPs, and base fluid, respectively.

The transient energy equation is presented in Eq. (13). The heat transfer by natural convection in the nanofluids can be neglected owing to the low NP volume fraction (less than 0.1%) and temperature (less than 100 °C) [37]. In this equation, q_r is the radiative heat flux, resulting in heating of the fluid from the incident solar radiation, and is defined in Eq. (14).

$$k\frac{\partial^2 T}{\partial y^2} - \frac{\partial q_r}{\partial y} = \rho c_p \frac{\partial T}{\partial t} \tag{13}$$

$$q_r = \int_{\lambda}\int_{4\pi} I_\lambda \, d\phi \, d\lambda \tag{14}$$

The boundary condition at the top surface of the collector is considered as heat transfer by natural convection, given by the following equation:

$$h_c\left(T_\infty - T(y,t)\big|_{y=0}\right) = -k\frac{\partial T(y,t)}{\partial y}\bigg|_{y=0} \tag{15}$$

where h_c is the convection heat transfer coefficient, which is assumed as 10 W/(m^2·K) for the typical natural convection from air; and T_∞ is the ambient temperature, taken as 20 °C. The boundary conditions for other surfaces are considered as adiabatic conditions, i.e., no heat flux is allowed to pass through, except for the transmitted radiation.

Finally, the collector efficiency η can be evaluated by [38]

$$\eta = \frac{mc_p(T_{average}\big|_{t=\Delta t} - T_{initial})}{AG\Delta t} = \frac{\rho H c_p(T_{average}\big|_{t=\Delta t} - T_{initial})}{G\Delta t} \tag{16}$$

where m is the nanofluid mass in the collector, $T_{average}$ is the average temperature of the nanofluid, $T_{initial}$ is the initial temperature of the nanofluid, A is the top cover area of the solar

collector, G is the solar flux incident upon the solar collector, Δt is the irradiation time, and H is the height of the solar collector.

2.4 Solution methodology

A finite difference method was used to solve the coupled RTE (Eq. (3)) and energy balance equation (Eq. (13)). The control volume integral method was chosen to derive the discretization equations. Accordingly, the spectral, time, and spatial spaces were divided into uniform nodes. Each interval was chosen to ensure that the iterations were consistently convergent and stable. First, the radiative heat flux with respect to y was determined through the numerical integration of Eq. (3) at time t_i. Second, the divergence of the radiative heat flux was incorporated into the energy balance equation to determine the temperature at time t_{i+1} using the implicit difference method. The new obtained temperature was subsequently reintroduced to the first step, and the above processes were repeated. Mesh refinement along the y direction was conducted to make the maximum variance in the temperature less than 0.01 °C. Table 1 lists the physical properties of water and silver for the calculation. The optical constants (such as n and κ) were obtained from references [39] and [40].

3. Experimental section

3.1 Silver-nanoparticle synthesis and characterization

Materials: Silver nitrate ($AgNO_3$, 99%), ascorbic acid ($C_6H_8O_6$, 99%), and trisodium citrate ($Na_3C_6H_5O_7$, 99%) were supplied by Aladdin (http://www.aladdin-e.com/) and used as received. Deionized water and redistilled water were used in the experiments.

Silver-nanoparticle synthesis: Silver NPs were synthesized by using ascorbic acid as a reductant and citrate as a stabilizer on the basis of Qin et al. [41] with minor changes. The specific synthesis process is as follows (Fig. 3). In vial A, 0.033 g of ascorbic acid and 0.264 g of trisodium citrate were dissolved in 100 mL of water with ultrasonic oscillation for 3 min. Then, 1.2 mL of a 0.1 M $AgNO_3$ solution was added to vial A and shaken for uniform mixing. Finally, the mixture in vial A was placed into a drying oven 30 °C to obtain complete reaction. The reaction solution was observed to change from colorless to yellow and then brown. After 30 min, no further change in color of the reaction solution occurred, indicating that the reaction was complete. The final solution in vial A was centrifuged at 10000 rpm for 10 min for analysis (Sigma2-16P centrifuge).

Characterization: Scanning Electron Microscopy (SEM) was used to observe the sizes and shapes of the silver NPs. SEM was performed with a Zeiss Supra 55 Sapphire electron microscope at a bias voltage of 30 kV. The average size and standard deviation of the silver NPs were determined from SEM images by averaging the diameters of at least 100 particles using a software application called Nano Measurer 1.2. As seen in the SEM images in Fig. 4 (a), the average size is ~53 nm. The optical absorbance spectra were measured at room temperature using a UV-Vis spectrophotometer (Pgeneral TU1901), where the nanofluid was held in quartz cuvettes with a

beam path length of 10 mm. The absorbance spectra of the silver nanofluid is shown in Fig. 4 (b) using water as the reference. One peak absorption wavelength was observed at 481 nm. The original solution was diluted to a volume fraction of 6.2 ppm and was applied in the following photothermal conversion experiments.

3.2 Photothermal conversion experiment

A schematic of the photothermal conversion test equipment is shown in Fig. 5. To examine the influence of the collector geometry, two test sections made of polymethyl methacrylate (PMMA) were fabricated. For model 1, the size of the inner box is 100 mm × 100 mm × 6 mm, and that of the outer one is 160 mm × 160 mm × 36 mm. For model 2, the dimension of the inner box is 50 mm × 50 mm × 48 mm, and that of the outer one is 110 mm × 110 mm × 80 mm. The space between the two boxes was filled with an insulating material to reduce heat loss, and the inner box contains the fluid under test. The details of these two collectors can be seen in Fig. 5 (b). K-type thermocouples were inserted into the middle of the nanofluid under test through the insulation material for model 1. For model 2, five thermocouples were installed at different heights (H = 15, 23, 31, 39, and 47 mm) to measure the temperature distribution. The thermocouples were connected to a data acquisition unit connected to a laptop for analysis. The light source was from a sunlight simulator using an artificial-sun analog transmitter (Jinzhou Sunshine Meteorological Science Co. Ltd., TRM-PD1 type). The intensity of the simulated sunlight was measured by a heat flow meter (Kyoto Electronics Mfg. Co., Ltd., HFM-215M). The initial temperature of the nanofluids for all experiments was 20 °C. The uncertainty in the measurement temperature was estimated to be ±0.2 °C.

3.3 Experimental results and comparison with numerical calculation results

The modeling temperature profiles including model 1 (H = 6 mm) and model 2 (H = 48 mm) are shown in Figs. 6 (a)–(c) for comparison with the experimental results. The experiments were conducted under the conditions described in Sections 3.1 and 3.2. To predict the performance of the experimental collector, the numerical calculation results are shown to be accurate with average deviations from the experimental results of 23.6% and 7.1% for model 1 and model 2, respectively. A possible source for these deviations might originate from the measuring error of the thermocouple due to instrumental errors and the effect of the solar radiation on the thermocouple. Another possible source may be the difference between the simulation model and experimental model since some assumptions were made to simplify the calculation. For example, the heat transfer by natural convection of the nanofluids was neglected owing to the low NP volume fraction (less than 0.1%) and temperature (less than 100°C). Furthermore, the Rayleigh approximation was applied to describe the absorption and scattering of the NPs when the size parameter $\alpha < 1$. For model 2, temperatures at different heights were measured to compare with the modeling results. The average temperatures of model 2 also matched the experimental results in Fig. 6 (c) well, demonstrating that good agreement is obtained between results from the experiment and present model.

For these two cases, the heat generation profiles are reflected in the temperature variation tendencies. With increasing time, the temperature gradually increases. For model 1, the average temperature difference between the modeling result and the experimental result is ~ 1.9°C， which is larger than that of model 2 (~ 0.2°C). This indicates that this model is more accurate for predicting the temperature profiles of the low-temperature collector since only heat loss by convection was considered in this model.

4. Results and discussion

Having demonstrated the validity of the model, this section will present the basic results for the DASC obtained from the model and discuss the effects of the variations in several operation parameters including the irradiation time, the height of the DASC, and the NP volume fraction on the collector efficiency or temperature.

Fig. 7 shows the transient temperature distribution at various depths and the temperature nonuniformity at the collector depth h. The transient temperature profiles show different trends at various depths, especially at the beginning. The gradient of the temperature change decreases as the depth increases for the first 400 s owing to the attenuation of radiation along the depth direction. As the radiation time increases, the heat loss of the fluid on the top surface increases owing to the increasing temperature, resulting in a decrease in the rate of temperature change. However, the relatively cool fluid at the bottom is heated by the increased solar radiation and conduction from the upper high-temperature fluid. These factors lead to an increase in the rate of temperature change for the fluid at the bottom. From Fig. 5 (b), it can be seen that the vertical variations in the temperature are small for the fluid both at the top and bottom, but a fast temperature decrease is observed in the middle part. The fluid at the top receives the highest radiation and has the highest temperature, which also results in the largest convective heat loss, leading to a small fluid temperature gradient at the top. For the fluid at the bottom, the low-temperature gradient is due to the low solar radiation owing to its attenuation. A nearly linear temperature decrease is observed for the fluids in the middle, contributed by both conduction and solar radiation.

4.1 Effect of the volume fraction

The variation in the collector efficiency as a function of the NP volume fraction f_v is shown in Fig. 8. In the visible-light region, the extinction coefficients are more sensitive to variations in the NP volume fraction at relatively low NP volume fractions. By increasing the NP volume fraction, the collector efficiency rapidly increases, meaning that the nanofluid absorbs much more solar energy. However, with a further increase in the volume fraction, the collector efficiency tends to approach a maximum value asymptotically, regardless of the radiation time. The attenuation of the solar radiation passing through the collector would be enhanced as the NP volume fraction increases, which in turn increases the collector efficiency. However, as the attenuation varies exponentially with the extinction coefficient (as shown in Eq. (3)), the efficiency initially

increases sharply at low concentrations but quickly reaches the asymptotic value. This suggests that a practical particle concentration should be used for any application by considering the tradeoff between the increase in the collector efficiency and increased NP cost. For different irradiation times, similar collection efficiency curves are observed, but the maximum efficiency decreases as the radiation time increases. This result indicates that an increase in the NP volume fraction is initially more beneficial for increasing the collector efficiency, and the enhancement in the collector efficiency would decrease gradually. For the case (i.e., silver nanofluids with an NP size of 10 nm and a collector height of 6 mm) considered here, a practical NP volume fraction would be 0.03% for achieving a collector efficiency of 90% of the maximum efficiency at different times, as shown in Fig. 8.

4.2 Effect of the solar collector height

The influence of the solar collector height on the collector efficiency is shown in Fig. 9. The collector efficiency increases as the collector height increases and then reaches a maximum value, which is different for different irradiation times. By increasing the collector height, the distance traveled by the solar radiation is increased owing to the attenuation of the spectral intensity, and more solar energy can be absorbed by the fluid, leading to higher efficiencies. However, the variation in the solar radiation intensity in the depth direction would decrease and then tend to a constant value owing to exponential attenuation, as indicated by Eq. (3). Therefore, when the collector height reaches a certain value, the collector efficiency would not be greatly enhanced any more, which is actually shown by the asymptotic behavior of the curves in Fig. 9. As such, the increase in the collector efficiency becomes very small when the collector height is sufficiently large. Again, a realistic collector height should be used for practical considerations. A practical collector height would be 10 mm for achieving a collector efficiency of 90% of the maximum efficiency considered here, as shown in Fig. 9.

4.3 Effect of the irradiation time

As shown in Fig. 10, the collector efficiency decreases as the irradiation time increases, which is associated with an increased heat loss. At the beginning, the temperature difference between the fluid and the atmosphere is small, resulting in a high collector efficiency. With an increase in the irradiation time, the fluid temperature increases, and the heat loss is enhanced, which leads to a reduction in the collector efficiency. As nanofluids with a higher NP volume fraction have stronger absorption of solar energy as well as a large heat loss, a higher NP volume fraction shows a larger rate of decrease in the efficiency, as shown in Fig. 10 (b). A nearly constant collector efficiency of ~20% is observed for water. Theoretically, when the heat loss and solar radiation energy are equivalent, the collector system reaches a steady state, and the efficiency would become zero, as no more solar energy is absorbed. Therefore, it is important to choose an optimal irradiation time in terms of the collector efficiency for solar utilization.

4.4 Effect of the solar intensity

The solar radiation intensity does not always match the conditions of AM = 1.5 owing to

variations in the location and weather. Hence, the effects of the solar flux are calculated, discussed, and shown in Fig. 11. When increasing the solar flux, the fluid temperature in the collector increases accordingly. For the same solar flux, the temperature gradient decreases as the irradiation time increased owing to the increased heat loss at a higher temperature. The high solar flux allows the collector to operate with a high efficiency over a wide temperature range. To obtain the same efficiency, a fluid irradiated with a higher solar flux should have a higher temperature. As it is beneficial for the working fluid to have a high temperature for subsequent utilization, it would be desirable to operate the solar collector at high solar radiation in terms of the temperature and collector efficiency.

4.5 Effect of the nanoparticle material

Finally, the collector temperatures and efficiencies of the DASC for different NP materials such as gold, silver, and titanium dioxide are compared for the same NP size (10 nm) and volume fraction (0.01%), as shown in Fig. 12. The results show that gold and silver nanofluids obtain a higher temperature and efficiency than those of a titanium dioxide nanofluid and water. The differences can be attributed to the various spectrum-dependent extinction coefficients of the working fluids. As a semiconductor material, titanium dioxide has a certain forbidden band gap, and if the photon energy is greater than the forbidden band gap, it will be absorbed and produce electron–hole pairs. The calculated critical absorption wavelength of titanium dioxide lies in the ultraviolet region, which is far from the solar intensity peak, as shown in Fig. 13 (c). For plasmonic NPs, the extinction coefficients of silver and gold NPs would be strongly enhanced at the LSPR frequency, which lies at ~500 and ~400 nm for gold and silver, respectively, as shown in Figs. 13 (a) and (b). The variations in the extinction coefficients in Fig. 13 can be attributed to the different optical constants of the absorbing medium for the same NP size or shape, NP volume fraction, and NP dispersion medium, which can be described by the complex refractive indexes by Eq. (5). The discrete experimental values of the complex refractive index obtained from references [39] and [40] were used to calculate the optical properties of the nanofluids. The complex refractive index can describe the process of light-wave propagation in a medium, which is the most important optical constant that varies for different materials. Fitting data based on the experimental data have been applied in the extinction coefficient calculation to reduce fluctuations.

Moreover, the majority of solar energy is in the visible-light region, which leads to a large enhancement in the temperature and efficiency of silver and gold nanofluids. Further, the wavelength at which the peak extinction coefficient is obtained for the gold nanofluid is closer to the wavelength of the peak solar intensity, resulting in a higher temperature increase and an efficiency greater than that of the silver nanofluid. The absorption region of water is mainly in the near infrared region, which is also far from the wavelength of the peak solar intensity, as for the titanium dioxide nanofluid in Fig. 13 (d). Therefore, under the same conditions, the gold and silver nanofluids show much better photothermal performance than the titanium dioxide nanofluid.

Considering the effect of the NP material, it is important to choose a material with suitable optical properties that match the solar spectral intensity in order to achieve the best solar absorption effect.

5. Conclusions

A numerical analysis was carried out to solve the RTE and energy balance equation to investigate the DASC performance and obtain the temperature distribution. Silver nanofluids were used as the working fluid in the solar collector. The optical properties of the nanofluids were obtained on the basis of the Rayleigh approximation. The effects of the NP volume fraction, collector height, irradiation time, solar flux, and NP material on the collector efficiency and temperature were evaluated.

The results show that the collector efficiency increases as the collector height and NP volume fraction increase and then reaches a maximum value. However, the collector efficiency decreases as the irradiation time increases owing to the enhanced heat loss. The high solar flux allows the collector to maintain a high efficiency over a wide temperature range, which is beneficial for subsequent energy utilization. There exist an optimal volume fraction and collector height for a DSAC. For the case (i.e., silver nanofluids with an NP size of 10 nm and a collector height of 6 mm) considered here, a practical NP volume fraction would be 0.03% for achieving a collector efficiency of 90% of the maximum efficiency at different times. Again, a realistic collector height (~ 10 mm) should be used for practical considerations. For different NP materials, the modeling results also show that silver and gold nanofluids possess higher collector efficiencies than that of a titanium dioxide nanofluid for the same volume fraction. Further improvements in the collector efficiency can be achieved by engineering the absorption spectrum of the working fluid to match the solar spectral intensity closely.

Acknowledgements

This work is financially supported by the National Natural Science Foundation of China (Grant No. 51322601), the Natural Science Funds of Heilongjiang Province for Distinguished Young Scholar (Grant No. JC2016009), the Science Creative Foundation for Distinguished Young Scholars in Harbin (Grant No. 2014RFYXJ004), and the Fundamental Research Funds for the Central Universities (Grant No. HIT. BRETIV. 201315).

References

[1] Rodhe H. A comparison of the contribution of various gases to the greenhouse effect[J]. Science, 1990, 248(4960): 1217.

[2] Likens G E, Bormann F H. Acid rain: a serious regional environmental problem[J]. Science, 1974, 184(4142): 1176-1179.

[3] Rodríguez-Sánchez D, Belmonte J F, Izquierdo-Barrientos M A, et al. Solar energy captured by a curved collector designed for architectural integration[J]. Applied Energy, 2014, 116: 66-75.

[4] Tian Y, Zhao C Y. A review of solar collectors and thermal energy storage in solar thermal

applications[J]. Applied Energy, 2013, 104: 538-553.
[5] Colangelo G, Favale E, Miglietta P, et al. Experimental test of an innovative high concentration nanofluid solar collector[J]. Applied Energy, 2015, 154: 874-881.
[6] Kalogirou S A. Solar thermal collectors and applications[J]. Progress in Energy and Combustion Science, 2004, 30(3): 231-295.
[7] Colangelo G, Favale E, De Risi A, et al. A new solution for reduced sedimentation flat panel solar thermal collector using nanofluids[J]. Applied Energy, 2013, 111: 80-93.
[8] Gude V G, Nirmalakhandan N, Deng S, et al. Low temperature desalination using solar collectors augmented by thermal energy storage[J]. Applied Energy, 2012, 91(1): 466-474.
[9] Abdelrahman M, Fumeaux P, Suter P. Study of solid-gas-suspensions used for direct absorption of concentrated solar radiation[J]. Solar Energy, 1979, 22(1): 45-48.
[10] Otanicar T P, Phelan P E, Prasher R S, et al. Nanofluid-based direct absorption solar collector[J]. Journal of Renewable and Sustainable Energy, 2010, 2(3): 033102.
[11] Ladjevardi S M, Asnaghi A, Izadkhast P S, et al. Applicability of graphite nanofluids in direct solar energy absorption[J]. Solar Energy, 2013, 94: 327-334.
[12] Verma S K,TiwariA K. Progress of nanofluid application in solar collectors: A review[J]. Energy Conversion and Management, 2015, 100: 324-346.
[13] Faizal M,Saidur R, Mekhilef S, et al. Energy, economic and environmental analysis of metal oxides nanofluidfor flat-plate solar collector[J]. Energy Conversion and Management, 2013, 76: 162-168.
[14] Tyagi H, Phelan P, Prasher R. Predicted efficiency of a low-temperature nanofluid-based direct absorption solar collector[J]. Journal of solar energy engineering, 2009, 131(4): 041004.
[15] Yiamsawas T, Mahian O, Dalkilic A S, et al. Experimental studies on the viscosity of TiO_2 and Al_2O_3 nanoparticles suspended in a mixture of ethylene glycol and water for high temperature applications[J]. Applied Energy, 2013, 111: 40-45.
[16] Prasher R, Bhattacharya P, Phelan P E. Thermal conductivity of nanoscale colloidal solutions (nanofluids)[J]. Physical Review Letters, 2005, 94(2): 025901.
[17] Krishnamurthy S, Bhattacharya P, Phelan P E, et al. Enhanced mass transport in nanofluids[J]. Nano Letters, 2006, 6(3): 419-423.
[18] Murshed S M S, Leong K C, Yang C. Investigations of thermal conductivity and viscosity of nanofluids[J]. International Journal of Thermal Sciences, 2008, 47(5): 560-568.
[19] Morteza K A. Influence of different design parameters and Al_2O_3-water nanofluid flow on heat transfer and flow characteristics of sinusoidal-corrugated channels[J]. Energy Conversion and Management, 2014, 88: 96-105.
[20] Myers P D, Alam T E, Kamal R, et al. Nitrate salts doped with CuO nanoparticles for thermal energy storage with improved heat transfer[J]. Applied Energy, 2016, 165: 225-233.
[21] Muhammad M J, Muhammad I A, Sidik N A C, et al. The use of nanofluids for enhancing the thermal performance of stationary solar collectors: A review[J]. Renewable and Sustainable Energy Reviews, 2016, 63: 226-236.
[22] Sarsam W S, Kazi S N, Badarudin A. A review of studies on using nanofluids in flat-plate solar collectors[J]. Solar Energy, 2015, 122: 1245-1265.
[23] Karami M, Bahabadi M A A, Delfani S, et al. A new application of carbon nanotubes nanofluid as working fluid of low-temperature direct absorption solar collector[J]. Solar Energy Materials and Solar Cells, 2014, 121: 114-118.
[24] Saidur R, Meng T C, Said Z, et al. Evaluation of the effect of nanofluid-based absorbers on

direct solar collector[J]. International Journal of Heat and Mass Transfer, 2012, 55(21): 5899-5907.
[25] Said Z, Sajid M H, Saidur R, et al. Evaluating the Optical Properties of TiO_2 Nanofluid for a Direct Absorption Solar Collector[J]. Numerical Heat Transfer, Part A: Applications, 2015, 67(9): 1010-1027.
[26] He Q, Wang S, Zeng S, et al. Experimental investigation on photothermal properties of nanofluids for direct absorption solar thermal energy systems[J]. Energy Conversion and Management, 2013, 73: 150-157.
[27] Chen M, He Y, Zhu J, et al. Enhancement of photo-thermal conversion using gold nanofluids with different particle sizes[J]. Energy Conversion and Management, 2016, 112: 21-30.
[28] Zhang H, Chen H J, Du X, et al. Photothermal conversion characteristics of gold nanoparticle dispersions[J]. Solar Energy, 2014, 100: 141-147.
[29] BandarraFilho E P, Mendoza O S H, Beicker C L L, et al. Experimental investigation of a silver nanoparticle-based direct absorption solar thermal system[J]. Energy Conversion and Management, 2014, 84: 261-267.
[30] Jain P K, Huang X, El-Sayed I H, et al. Noble metals on the nanoscale: optical and photothermal properties and some applications in imaging, sensing, biology, and medicine[J]. Accounts of Chemical Research, 2008, 41(12): 1578-1586.
[31] Matthew R, Cobley C M, Jie Z, et al. Controlling the synthesis and assembly of silver nanostructures for plasmonic applications.[J]. Chemical Reviews, 2011, 111(6):3669-712.
[32] Duan H, Xuan Y. Synthesis and optical absorption of Ag/CdS core/shell plasmonic nanostructure[J]. Solar Energy Materials and Solar Cells, 2014, 121: 8-13.
[33] Modest M F. Radiative heat transfer[M]. Academic Press, 2013.
[34] Tien C L. Thermal radiation in packed and fluidized beds[J]. Journal of Heat transfer, 1988, 110(4b): 1230-1242.
[35] Putnam S A, Cahill D G, Braun P V, et al. Thermal conductivity of nanoparticle suspensions[J]. Journal of Applied Physics, 2006, 99(8): 084308.
[36] Chen G. Nanoscale energy transport and conversion[M]. Oxford university press, 2005.
[37] Ho C J, Chen M W, Li Z W. Numerical simulation of natural convection of nanofluid in a square enclosure: effects due to uncertainties of viscosity and thermal conductivity[J]. International Journal of Heat and Mass Transfer, 2008, 51(17): 4506-4516.
[38] Chen M, He Y, Zhu J, et al. An experimental investigation on sunlight absorption characteristics of silver nanofluids[J]. Solar Energy, 2015, 115: 85-94.
[39] Sadao A. Handbook of optical constants of metals[M]. World Scientific,2014.
[40] Hale G M, Querry M R. Optical constants of water in the 200-nm to 200-μm wavelength region[J]. Applied Optics, 1973, 12(3): 555-563.
[41] Qin Y, Ji X, Jing J, et al. Size control over spherical silver nanoparticles by ascorbic acid reduction[J]. Colloids and Surfaces A: Physicochemical and Engineering Aspects, 2010, 372(1): 172-176.

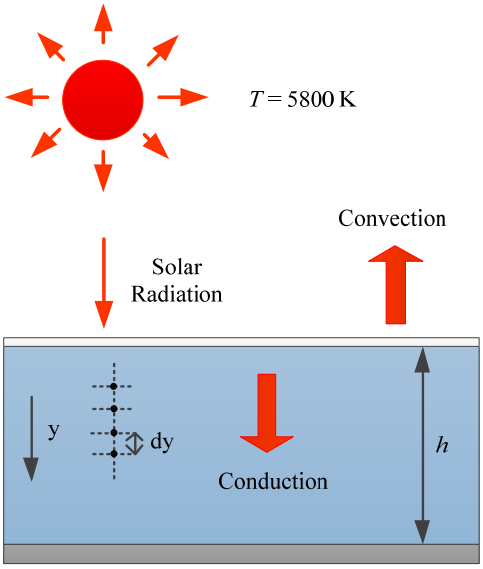

Fig.1 Schematic for the model formulation of a 1-D direct absorption solar collector with a transparent top (y = 0) and other three adiabatic surfaces

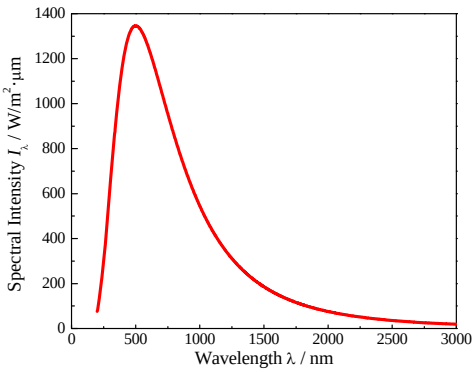

Fig.2 Spectral radiant intensity versus wavelength

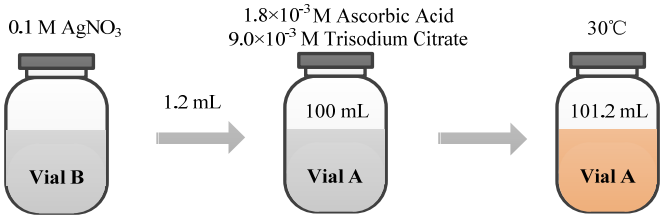

Fig.3 Synthetic procedure for Ag nanoparticles

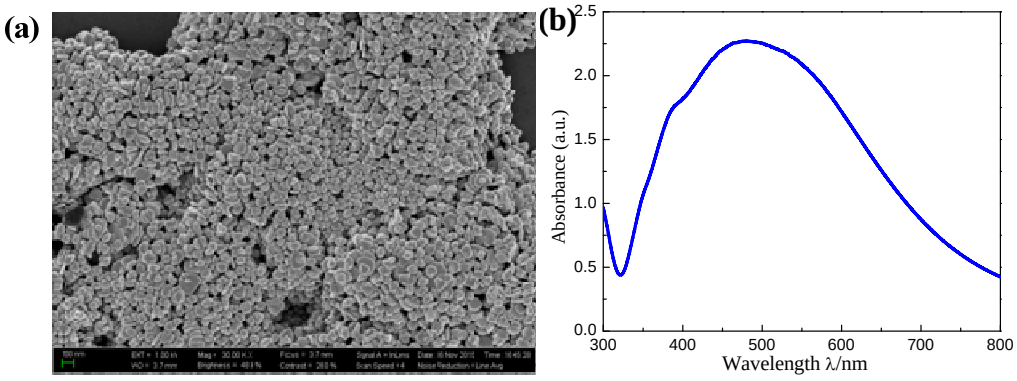

Fig.4 Silver nanoparticles' characterization: (a) SEM images of Ag nanoparticles;(b) Absorbance spectra of Ag nanofluid

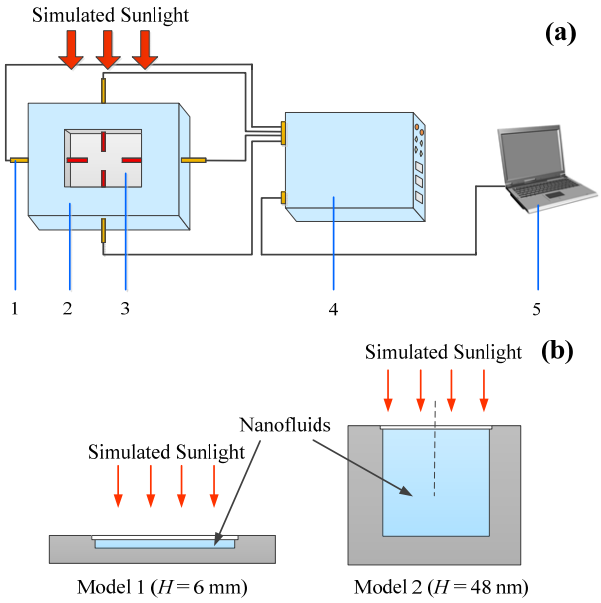

Fig.5 Schematic diagram of photo-thermal conversion test equipment
(1-thermocouples; 2-PMMA boxes; 3-nanofluid; 4-data acquisition unit; 5-laptop)

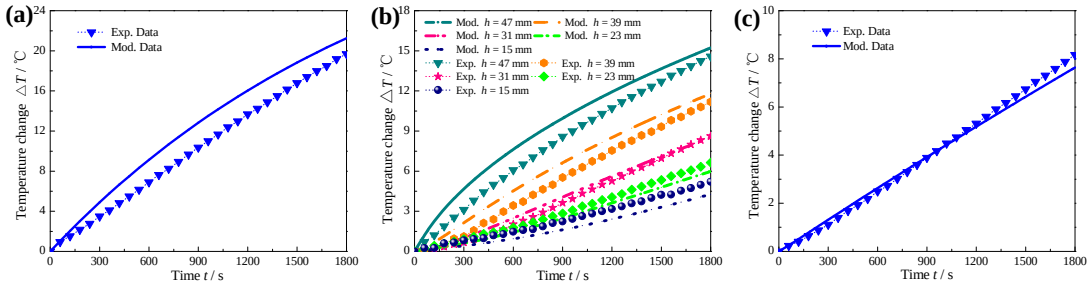

Fig.6 Comparison of modeling and experimental temperature distribution with irradiation time for Ag nanofluids: (a) average temperature change with irradiation time for model 1; (b) different height temperature change with irradiation time for model 2; (c) average temperature change with irradiation time for model 2

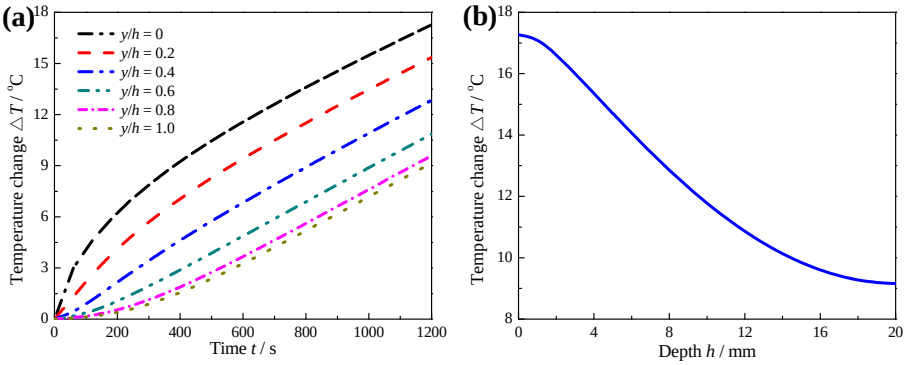

Fig.7 Temperature distribution in the DASC (Ag nanofluid: D = 10 nm, H = 20 mm and f_v = 0.02%) (a) Temperature variation with irradiation time at different depths; (b)Temperature variation with depth at the irradiation time of 1200 s

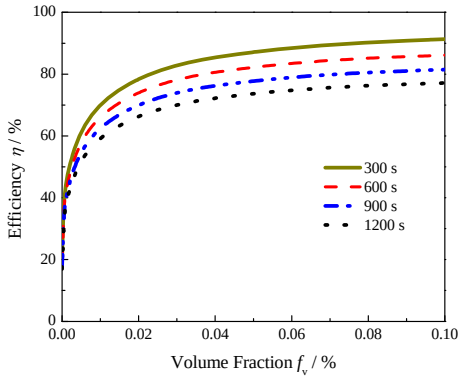

Fig.8 Collector efficiency as a function of volume fraction with various irradiation time (Ag nanofluid: D = 10 nm and H = 6 mm)

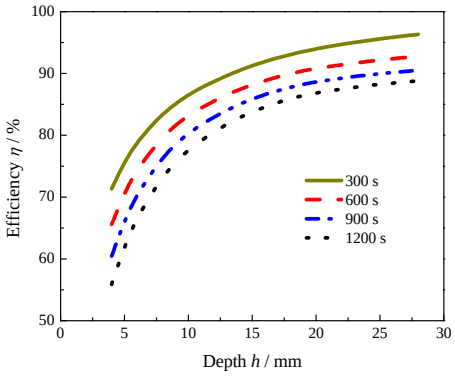

Fig.9 Collector efficiency as a function of collector height with various irradiation time (Ag nanofluid: D = 10 nm and f_v = 0.02%)

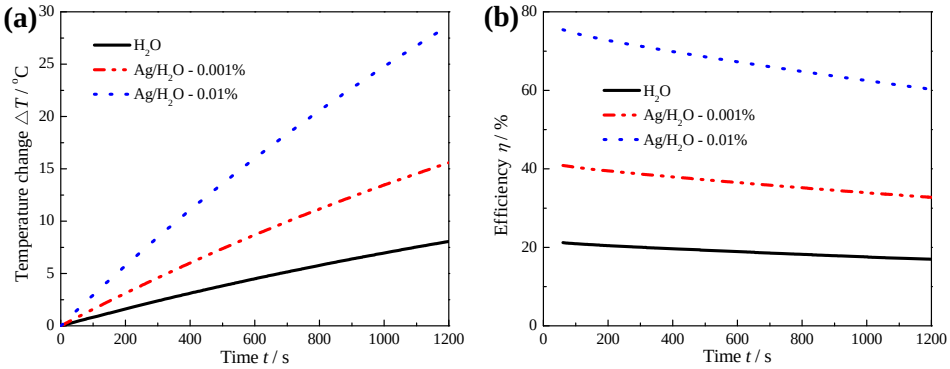

Fig.10 Collector efficiency as a function of the irradiation time (Ag nanofluid: D = 10 nm and H = 6 mm)

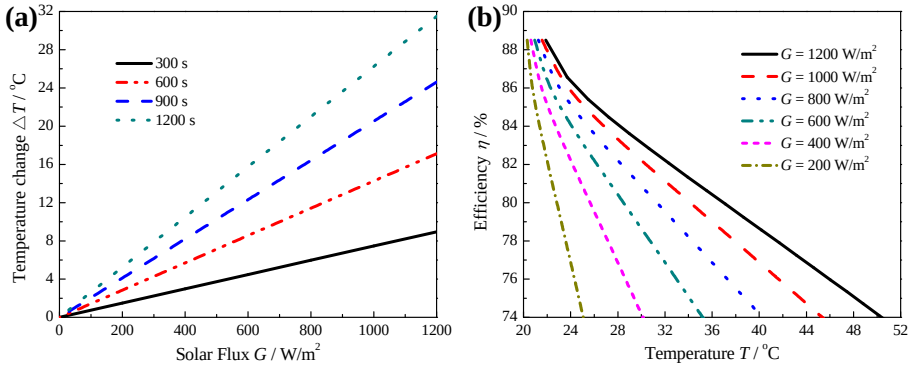

Fig.11 Effects of solar flux on temperature and collector efficiency (Ag nanofluid: D = 10 nm, H = 8 mm and f_v = 0.02%): (a) Temperature varies with solar flux; (b) Collector efficiency varies with temperature

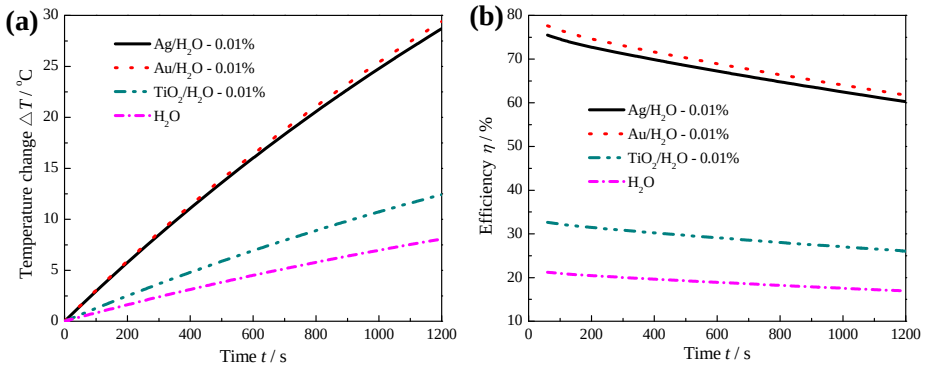

Fig.12 Effects of different nanoparticles' materials for temperature and collector efficiency (D = 10 nm, H = 6 mm and f_v = 0.01%): (a) Temperature varies with time; (b) Collector efficiency varies with time

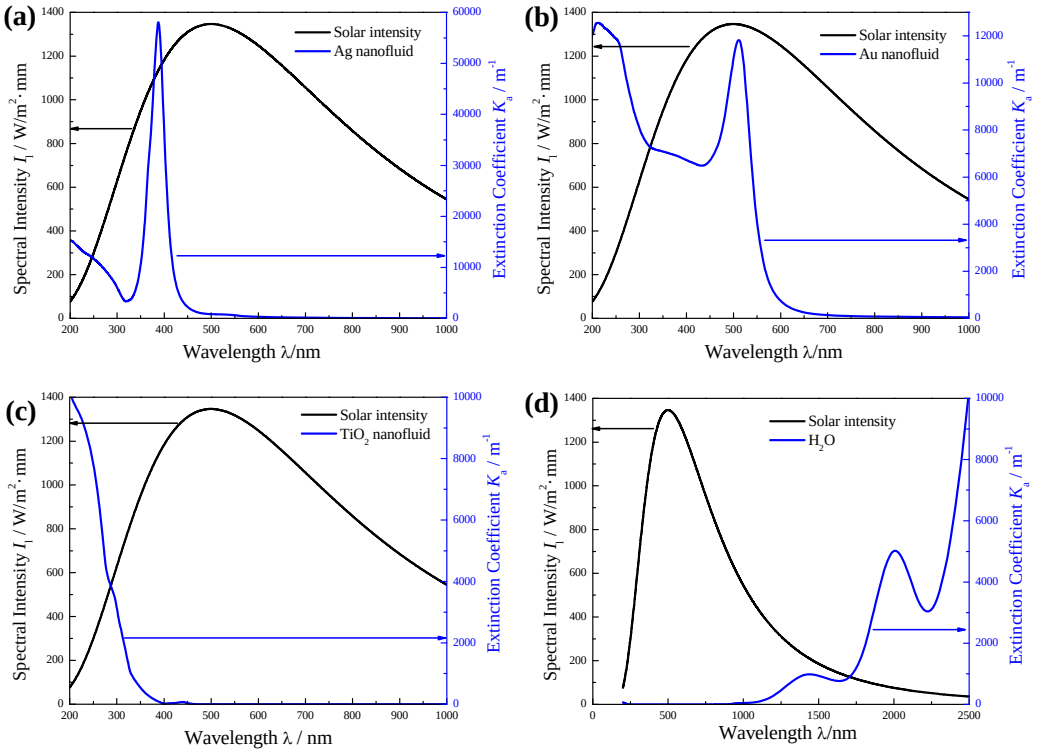

Fig.13 Extinction coefficient curves of Ag, Au, TiO_2 nanofluids and water (D = 10 nm and f_v = 0.01%)